Energy Conversion and Management 315 (2024) 118806

Contents lists available at ScienceDirect

Energy Conversion and Management

journal homepage: www.elsevier.com/locate/enconman

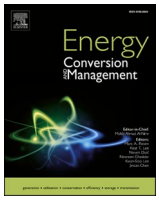

Constructal design of biogas fired Stirling engine-based micro combined heat and power system using a novel polytropic endothermic/exothermic thermal model

Minjie Yu, Haichuan Cui, Lei Xu, Zhichun Liu, Wei Liu *

School of Energy and Power Engineering, Huazhong University of Science and Technology, Wuhan 430074, China

ARTICLE INFO

Keywords:
Combined heat and power
Stirling engines
Biomass
Polytropic endothermic/exothermic process
Constructal optimization
Inclined-flow regenerator

ABSTRACT

Renewable energy-driven micro combined heat and power systems offer a clean and efficient solution for energy supply in residential and commercial buildings. This paper presents a novel model for a biogas-fired Stirling engine-based micro combined heat and power system, and establishes the mathematical relationships between geometric and operational parameters of components and the system's thermal-electric performance. To improve the accuracy of system performance prediction, the model meticulously considers the intricate heat-to-work conversion and thermal energy transfer processes, incorporating the finite heat transfer capacity and polytropic endothermic/exothermic processes in the heat exchangers of the prime mover. The reliability of the system model is verified, and constructal theory is introduced to optimize the critical geometric variables of thermal energy transfer components within the system based on the new model. The results demonstrate that compared to the performance before optimization, the electrical power output of the system increases by 142.8 %, while heat output efficiency and overall efficiency increase by 20.5 % and 10.5 %, respectively. This work provides a new approach and perspective for the mathematical modeling, performance assessment, and optimization design of Stirling engine-based micro combined heat and power systems.

1. Introduction

The continuous development of society and economy has led to a rapid increase in global energy demand. Within total energy consumption, energy utilization within buildings accounts for 30–45 % [1]. Heat and electricity stand out as the primary forms of energy consumed within buildings. The quest to produce and deliver these two energy forms for buildings in a simple and efficient manner has emerged as a prominent topic in energy research, representing a critical aspect for both energy conservation and security [2]. Combined heat and power (CHP) systems serve as devices adept at supplying both heat and electricity with high efficiency, which can exceed 90 % after optimization [3]. As a distributed energy integration system, the CHP system possess the flexibility to adjust power generation capacity and thermal-electric output ratio based on users' needs, thereby effectively alleviating the strain on grid load stability [4]. Moreover, being situated in close proximity to users, CHP systems mitigate the heightened energy dissipation associated with long-distance thermal-electric transmission [1]. Consequently, CHP systems have emerged as a promising solution for meeting the energy demands of buildings.

CHP systems typically comprise a prime mover, a generator, and several essential energy supply and transfer components [5]. These systems are broadly classified into three sizes based on electrical power output: micro (3–15 kW), small (15–100 kW), and large (over 100 kW) [6]. Micro- and small-CHP systems, tailored to meet the electricity demands of residential and small commercial buildings, hold the most promising applications. Currently, various prime movers [7] employed for converting heat into work in CHP systems include steam engines [8], gas turbines [9], internal combustion engines [10], ORCs [11], thermophotovoltaic devices [12], fuel cells [13], geothermal systems [14], and Stirling engines [15]. Each type of CHP system, depending on the prime mover used, presents distinct advantages in different energy types and application scenarios. Stirling engines, renowned for their high theoretical thermal efficiency (equivalent to Carnot cycle efficiency) and moderate electrical power output range (1–50 kW) [6], are especially suitable for micro- and small-CHP systems catering to building energy needs. Additionally, Stirling engine-based CHP systems offer benefits such as low noise, environmentally friendly operation, and minimal

* Corresponding author.
E-mail address: w_liu@hust.edu.cn (W. Liu).

https://doi.org/10.1016/j.enconman.2024.118806
Received 3 April 2024; Received in revised form 9 July 2024; Accepted 12 July 2024
Available online 16 July 2024

maintenance costs [16]. On the other hand, historically, CHP systems primarily relied on fossil fuels like coal, oil, and natural gas as their main sources of primary energy [17]. However, with increasing awareness of the environmental pollution associated with fossil fuel use, cleaner and renewable energy sources like solar energy, geothermal energy, hydrogen, and biomass fuels have become preferred primary energy sources for CHP systems [18]. Among these, biomass fuels, with their abundant reserves, low cost, and high energy supply temperatures, are particularly suitable for ensuring the stable and efficient operation of Stirling engine-based CHP systems [19]. In this study, the primary energy source utilized is a gaseous biomass fuel: biogas, offering the advantage over solid biomass fuels of being less likely to cause fouling in the system [6]. Nevertheless, despite the impressive theoretical efficiency and environmental friendliness demonstrated by renewable energy-driven Stirling engine-based CHP systems, their commercial application remains limited. This limitation primarily arises from various irreversible heat transfer and flow losses resulting from poor design of system components, leading to suboptimal operational performance and high unit costs of thermal-electric output [20]. Therefore, optimizing the design of CHP systems is paramount to enhancing their actual thermal-electric output performance and fostering their commercial development.

To explore pathways for optimizing the comprehensive thermal-electric performance of Stirling engine-based CHP systems, a series of experimental tests and mathematical modeling have been undertaken to analyze operational characteristics and the impact of parameters on systems. Park et al. [21] designed and tested a kW-class free-piston Stirling engine-based CHP system to analyze its dynamic operational characteristics. The dual-opposed linear alternator in the free-piston Stirling engine effectively addresses the mechanical force issues typically encountered between the dual pistons. Chen et al. [22] incorporated thermophotovoltaic technology into a Stirling engine-based CHP system to further enhance its performance. Taguchi method was applied to optimize the fuel composition, fuel–air ratio, and flowrate mixture within the system. Subsequently, they also employed the Taguchi method to improve the performance of a Stirling engine-based CHP system integrated with a fluidized-bed biofuel unit, optimizing parameters such as sand height, air flow rate, and biomass feed rate [23]. Similarly, Schneider et al. [24] conducted experimental research on a fluidized-bed-fired Stirling engine-based CHP system. They tested the effects of operational parameters like fuel flow rate, excess air ratio, and cooling temperature on system performance, achieving 13–15 % electrical efficiency and over 85 % overall fuel utilization. Aunon-Hidalgo et al. [25] were the first to establish a Stirling engine-based CHP system that includes solar photovoltaic and thermal units, where the Stirling engine unit achieved a maximum efficiency of 93.9 %, meeting 75.6 % of the total residential thermal and electrical demand. These experimental investigations yield intuitive and accurate results, playing an indispensable role in the development and validation of CHP system technology. However, due to long testing cycles and high economic costs, they are unsuitable for large-scale parameterized research and optimization with high data demands, especially when involving changes in geometric parameters of the system.

In contrast, mathematical modeling methods are simple and efficient, and with continuous model refinements, their accuracy can progressively approximate experimental approaches, thereby significantly contributing to the investigation and optimization of Stirling engine-based CHP systems. Mehregan et al. [26] combined a proton exchange membrane fuel cell with a Stirling engine for CHP applications, establishing mathematical models for both prime movers using thermodynamic methods. They examined the impact of parameters such as engine speed, temperature, and fuel cell heat flux density on overall system performance and optimized the system using a multi-objective genetic algorithm. Qiu et al. [27] employed finite element and computational fluid dynamics methods to optimize the structural design of components in a free-piston Stirling engine-based CHP system. They also utilized Sage software to develop a one-dimensional thermodynamic model of the Stirling engine, analyzing the dynamic characteristics of the piston and rocking mode. Gonzalez-Pino [5] proposed a semi-empirical dynamic model for a natural gas-fired Stirling engine-based micro-CHP system, considering the dynamic behavior during startup, normal operation, and cooling phases. This model was derived based on mass and energy conservation principles but required experimental determination of empirical parameters for solution. Subsequently, Zhu et al. [28] used this dynamic model to conduct a techno-economic analysis of a CHP system integrating a Stirling engine, hybrid photovoltaic-thermal collectors, and energy storage. They also [29] developed a hybrid model based on thermoacoustic theory to simulate a free-piston Stirling engine-based CHP system, employing acoustic impedance matching and Sage to emulate the acoustically resonant system. The model's accuracy was validated through experiments. These models have substantially enriched our comprehension of the steady and transient operation characteristics of CHP systems, as well as the influence mechanisms of internal operational parameters. However, most of these models are semi-empirical, relying on experimental data, and lack rigorous modeling of the intricate energy conversion and coupled thermal energy transfer processes among subsystems or components within the system. This limitation hampers parameterized research and optimal design of the system's critical geometric structures, despite the significant impact these parameters have on the overall performance of CHP systems. Consequently, to bridge this gap, this paper establishes a novel Stirling engine-based micro-CHP system model from the perspectives of thermodynamics and heat transfer theory, taking into account the detailed influence of geometric configurations on internal heat-to-work conversion and thermal energy transfer processes.

In mathematical modeling of CHP systems, effective evaluation of the internal heat-to-work conversion performance of its prime mover is essential for predicting the system's overall output performance precisely. Currently, the most commonly used modeling method for Stirling engines is second-order numerical analysis. Compared to other methods, it offers moderate modeling complexity, shorter computation time cycles, and can achieve higher prediction accuracy by coupling various irreversible energy loss correction terms [30]. In second-order analysis, the Stirling engine is typically simplified into five components: two working chambers (compression chamber and expansion chamber) and three heat exchangers (heater, regenerator, and cooler) [31]. As researchers deepen their understanding of operation characteristics for Stirling engines, thermal models based on isothermal [32], adiabatic [33], and polytropic [34] compression/expansion processes have been successively proposed. Improved versions based on these three types of models have also been extensively developed, gradually enhancing the accuracy of engine performance prediction. However, all previous second-order models have been formulated and developed based on various assumptions concerning the compression and expansion processes within the working chambers. They all share the common assumption that the working gas experiences isothermal endothermic and exothermic processes within the heater and cooler, respectively. This overlooks the effectiveness of heat transfer between the internal heat exchangers and external heat sources. In practical endothermic and exothermic processes, the heat transfer capacity of the heater and cooler is limited. With the periodic changes in the mass flow rate of the working gas entering the heater and cooler during the cycle, the temperature of the gas within the heat exchangers cannot remain constant. Instead, it undergoes actual variations that align more closely with complex polytropic processes. Therefore, this paper, for the first time according to the authors' knowledge, replaces the isothermal endothermic and exothermic processes with polytropic ones, and, in conjunction with the previous analysis of polytropic working processes, establishes a new Stirling engine-generator submodel incorporating polytropic endothermic/exothermic and compression/expansion processes (SPEC) for theoretical analysis of CHP systems.

Based on the considerations mentioned above, the objective of this

study is to construct a novel Stirling engine-based micro-CHP system model that meticulously considers the complicated heat-to-work conversion and thermal energy transfer processes within the system, using the new SPEC analysis. This model aims to establish mathematical relationships between the system's comprehensive thermal-electric performance and the geometric configurations of its components, serving as an efficient and convenient theoretical tool for the investigation and optimization of important structural parameters within micro-CHP systems. Various subsystems are formulated and integrated using principles of mass and energy conservation, as well as heat transfer theory, to determine key operational parameters (such as fuel mass flow rate, temperatures of hot flue gas, water, and exhaust gas) of the system and significant thermal-electric performance criteria. By rigorously validating the predictive accuracy of the core heat-to-work conversion performance within the system, the reliability of the proposed micro-CHP system model has been demonstrated. Subsequently, the crucial geometric configurations of the thermal transfer components (regenerator, heater, cooler, and heating boiler) within the system are optimized based on the new micro-CHP system model. To enhance the rationality of the optimization results, the efficient constructal theory [35] in engineering design and optimization is introduced. By considering the overall geometric constraints and local geometric coupling effects of each component, synergistic optimization of geometric parameters is achieved [36]. In contrast to traditional optimization methods, constructal theory focuses more on the evolution of optimal geometry for achieving best performance in finite-size systems, rather than solely on performance itself [37]. Additionally, in constructal design of the regenerator, considering the significant influence of regenerator characteristics on the Stirling engine's heat-to-work conversion performance [38], a design concept of inclined-flow regenerator was previously proposed by the author [39] to achieve higher comprehensive heat and mass transfer performance compared to traditional cross-flow [40] and parallel-flow [41] regenerators. The potential of inclined-flow regenerators to improve Stirling engine performance has been preliminarily demonstrated [42]. Here, their feasibility in enhancing the comprehensive thermal-electric performance of micro-CHP systems will be further validated. Overall, the main innovations of this work include:

(1) Construction of a novel Stirling engine-based micro-CHP system model that meticulously considers the influence of geometric configurations of components on system's complex heat-to-work conversion and thermal energy transfer processes.
(2) Proposal of a new Stirling engine-generator submodel incorporating polytropic endothermic/exothermic and compression/expansion processes.
(3) Optimization of crucial geometric parameters of thermal energy transfer components within the micro-CHP system based on constructal theory.
(4) Investigation and comparison of the effects of regenerators with different matrix structure types on the performance of Stirling engine-based micro-CHP systems.

2. Description of Stirling engine-based micro combined heat and power systems

The component composition of the Stirling engine-based micro-CHP system is depicted in Fig. 1. The system primarily comprises a Stirling engine, generator, combustion chamber, heater, and gas, water, and electrical networks. During system operation, a mixture of biogas and air, in a specified ratio, is ignited in the combustion chamber, releasing heat. A portion of this heat is transferred to the Stirling engine's heater via convective and radiative heat transfer, after which the hot flue gas enters the heating boiler shell side to exchange heat with water inside the pipes, significantly cooling down before exiting the boiler as exhaust gas. The heat entering the Stirling engine through the heater is converted into mechanical energy of the piston within the engine, further

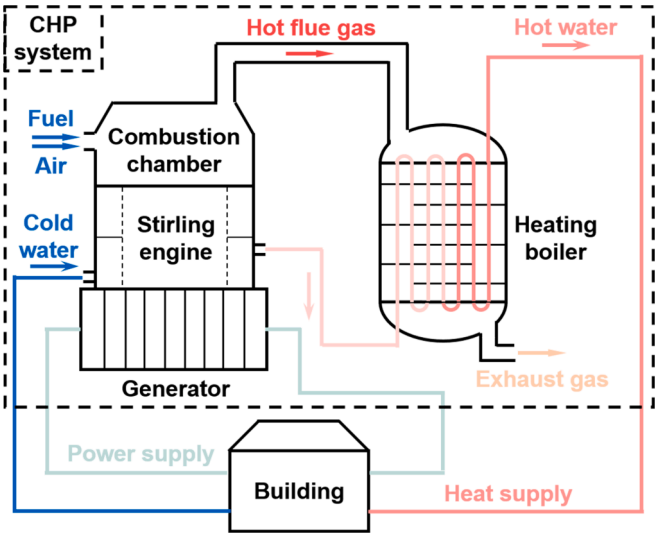

Fig. 1. Component composition of the Stirling engine-based micro-CHP system.

transformed into electrical energy within the generator, and supplied to the building via the local power grid. On the other hand, cold water from the building's supply network initially enters the external water jacket of the Stirling engine's cooler to cool the working gas inside the cooler tubes, and the warmed water proceeds to flow into the heating boiler tubes, where it absorbs additional heat from the external flue gas. Finally, the hot water exits the heating boiler and flows into the building through the water circulation network.

When compared to a standalone condensing boiler, the CHP system can not only provide sufficient heat output but also convert some of this heat into higher-grade electrical power, leading to greater economic benefits. Moreover, by utilizing clean biomass energy sources like biogas to meet both electricity and heat needs within buildings, CHP systems also offer enhanced environmental friendliness. A significant concern is that the Stirling engine-based CHP system may incur higher installation and maintenance costs compared to a standalone condensing boiler. However, the extra cost might be offset by the additional economic benefits derived from the electrical power generated by the Stirling engine.

2.1. Subsystems in the combined heat and power system

Based on the mass flow of various fluids and the energy transfer and conversion processes during the operation of the Stirling engine-based micro-CHP system described above, the system can be simplified into three subsystems: the combustion chamber (CC) subsystem, the Stirling engine-generator (SE-G) subsystem, and the heating boiler (HB) subsystem, as depicted in Fig. 2. Assuming full combustion of the biogas and disregarding energy losses in the gas, water, and electrical networks, Fig. 2 also illustrates the energy flows between subsystems. In the figure, $\dot{H}_{fuel}$ and $\dot{H}_{air}$ denote the enthalpies of the biogas fuel and air entering the CC, respectively, while $\dot{Q}_{conv}$ and $\dot{Q}_{radi}$ are the heat transferred from the hot flue gas to the SE-G through convective and radiative means. P_{el} and $\dot{E}_{loss}$ denote the electrical power output and energy losses of the SE-G. $\dot{H}_{HG}$ and $\dot{H}_{exh}$ are the enthalpies of the hot flue gas and exhaust gas, respectively, while $\dot{H}_{w,i}$, $\dot{H}_{w,md}$ and $\dot{H}_{w,o}$ represent the enthalpies of the water at the inlet and outlet of the Stirling engine cooler's external water jacket and at the HB's outlet. In the following section, various subsystems of the micro-CHP system will be mathematically modeled and integrated based on the energy flows between them, as well as the mass and energy conservation relationships within each subsystem.

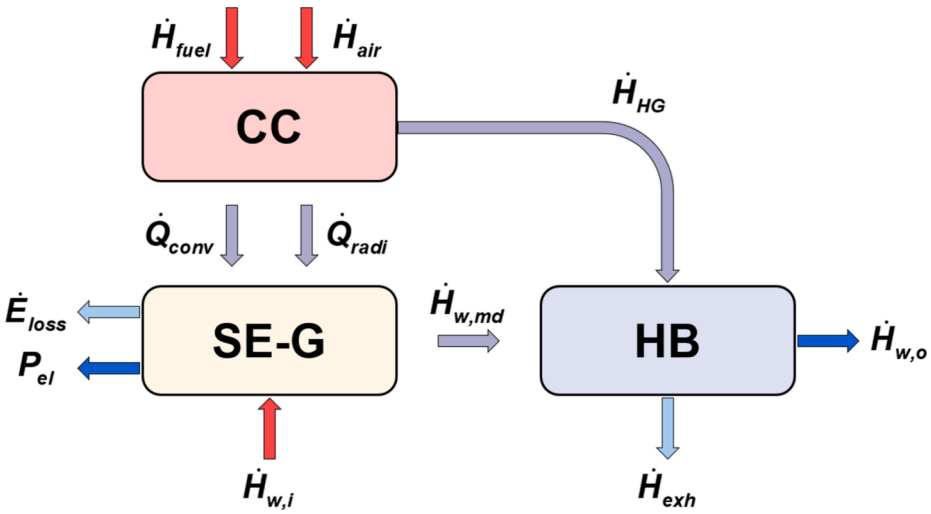

Fig. 2. Three subsystems and energy flows between subsystems in the CHP system.

2.2. Stirling engine-Generator subsystem modeling

Herein, a new thermal model incorporating polytropic endothermic/exothermic and compression/expansion processes (SPEC) is proposed for the SE-G subsystem, where the physical field distribution and energy transfer are illustrated in Fig. 3(a). In this model, subscripts c, k, r, h, and e respectively denote the compression chamber, cooler, regenerator, heater, and expansion chamber of the Stirling engine, while double subscripts ck, kr, rh, and he represent the interfaces between adjacent components. V denotes the volume of each component, and p, T, and m respectively indicate the pressure, temperature, and mass or mass flow rate of the working gas within the components. Q and W represent the heat absorbed from and work done on the external environment by each component, respectively. In previous classical analyses, including isothermal, adiabatic, and polytropic approaches, the focus of modeling was primarily on the assumptions regarding the compression and expansion processes within the working chambers, overlooking the effectiveness of endothermic and exothermic processes within the heat exchangers. In these models, the temperature of the gas inside the heater and cooler was assumed to remain constant throughout the cycle, i.e., T_h = Constant, T_k = Constant, disregarding the limited heat transfer capacity of the heater and cooler in actual heat exchange processes. Therefore, distinct from all previous second-order thermal models, the present SPEC model substitutes the isothermal endothermic/exothermic processes within the engine to be polytropic ones. Additionally, in the derivation of the original differential equation system, the pressure drop across each heat exchanger and the imperfect regenerative process within the regenerator are taken into account, thereby correcting the instantaneous pressure values within each component and the outlet temperature values of the gas at both ends of the regenerator. In summary, the important assumptions underlying the derivation of the differential equation systems in the present model are as follows:

(1) The compression and expansion processes within the working chambers are polytropic.
(2) The endothermic and exothermic processes within the heater and cooler are polytropic.
(3) The instantaneous pressure of each component is different.
(4) The effectiveness of the regenerator is less than 1.

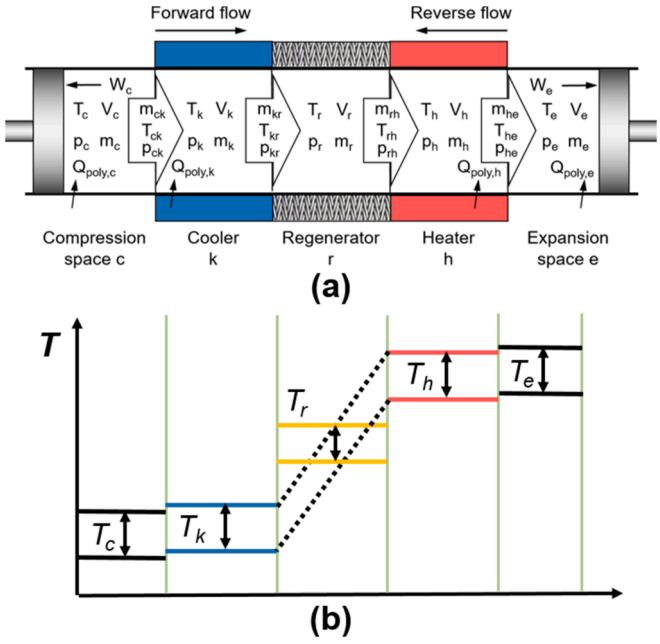

Fig. 3. Physical field distribution and energy transfer within the new SPEC model.

Therefore, in the current model, the temperature profiles of the various components of the Stirling engine are illustrated in Fig. 3(b). Unlike in previous second-order models, where the gas temperature within the three heat exchangers remains constant, in the new model, due to the polytropic feature of the working and heat transfer processes within the compression/expansion chambers and heater/cooler, the instantaneous average temperature of the gas within the five engine components undergoes periodic variations within distinct ranges.

Based on the mass and energy conservation in the current model, the detailed derivation process of the SE-G submodel is provided in Supplementary Material with Eqs. (S1)-(S60). Consequently, the instantaneous heat transfer of the gas within the heater, cooler, and regenerator to external heat sources or matrix can be determined as:

$$dQ_{poly,k} = c_v \frac{V_k dp_k}{R} + m_{kr} c_p T_{kr} - m_{ck} c_p T_{ck} \tag{1}$$

$$dQ_{poly,h} = c_v \frac{V_h dp_h}{R} + m_{he} c_p T_{he} - m_{rh} c_p T_{rh} \tag{2}$$

$$dQ_r = c_v \frac{V_r dp_r}{R} + m_{rh} c_p T_{rh} - m_{kr} c_p T_{kr} \tag{3}$$

where c_v, c_p, and R signifies the specific heat at constant volume of the

gas, specific heat at constant pressure of the gas, and gas constant, respectively.

The instantaneous ideal work performed within the compression chamber and expansion chamber respectively is:

$$dW_c = p_c dV \tag{4}$$

$$dW_e = p_e dV \tag{5}$$

Therefore, based on the derived instantaneous heat transfer rates and ideal work, and accounting for the various energy losses during system operation, the actual electrical power output of the SE-G subsystem is calculated as follows (ignoring energy losses within the generator):

$$P_{ac} = W_{ac} f - P_{hy} = \left\{ \int \left\{ (dW_c + dW_e) - dW_{pd} - dW_{FSTandmech} \right\} \right\} f - P_{hy} \tag{6}$$

where P_{hy} represents the power loss due to gas spring hysteresis, dW_{pd} denotes the power loss caused by pressure drop within the heat exchangers, and $dW_{FST\ and\ mech}$ indicates the power loss resulted from the finite motion of the piston and mechanical friction, with their expressions detailed in Eqs. (S70), (S66), and (S67) in Supplementary Material, respectively. W_{ac} stands for the actual cyclic work output of the engine without including the loss due to gas spring hysteresis, while f represents the engine frequency.

The actual heat absorption and release rates are as follows:

$$\dot{Q}_{h,ac} = Q_{h,ac} f = \left\{ \int \left(dQ_{poly,h} + dQ_{r,loss} + dQ_{cond,r} + dQ_{cond,d} + dQ_{leak} \right) \right\} f \tag{7}$$

$$\dot{Q}_{k,ac} = Q_{k,ac} f \left\{ \int \left(dQ_{poly,k} - dQ_{r,loss} - dQ_{cond,r} - dQ_{cond,d} - dQ_{leak} \right) \right\} f \tag{8}$$

where the terms $dQ_{r,loss}$, $dQ_{cond,r}$, $dQ_{cond,d}$, and dQ_{leak} represent the heat losses caused by imperfect regeneration, heat conduction through the regenerator wall, heat conduction through the displacer wall, and gas leakage, respectively, which are calculated using Eqs. (S62)-(S65) in Supplementary Material. $Q_{h,ac}$ and $Q_{k,ac}$ denote the actual cyclic heat absorption and heat release of the engine, respectively.

As a result, the thermal efficiency of the subsystem is calculated as:

$$\eta_{ac} = \frac{P_{ac}}{\dot{Q}_{h,ac}} \tag{9}$$

2.3. Combustion chamber subsystem modeling

In a biogas fired CHP system, the fuel's mass flow rate and the corresponding flue gas temperature during steady-state operation need to be adjusted based on the system's heat demands under specific geometries and conditions. Additionally, in the control of Stirling engine-based CHP systems, the heater wall temperature (T_H) of the Stirling engine is typically maintained around a reasonably expected value to ensure the safe and efficient operation of the engine. Therefore, in modeling the CC subsystem, based on the given heater wall temperature (T_H) and its corresponding heat demand, energy conservation and thermal energy transfer equations are applied to solve for the mass flow rates of fuel and air entering the CC, as well as the temperature of the flue gas.

The energy conservation equation for the CC subsystem is:

$$\dot{H}_{fuel} + \dot{H}_{air} = \dot{H}_{HG} + \dot{Q}_{h,ac} \tag{10}$$

In the above equation, $\dot{H}_{fuel}$, $\dot{H}_{air}$, and $\dot{H}_{HG}$ represent the enthalpy of the fuel, air, and hot flue gas, respectively. The enthalpy of the fuel and air entering the CC are:

$$\dot{H}_{fuel} = LHV \cdot \dot{m}_{meth} + \sum h_{comp} \dot{m}_{comp} \tag{11}$$

$$\dot{H}_{air} = \dot{m}_{air} \cdot h_{air} \tag{12}$$

where LHV represents the lower heating value of effective energy component (methane, CH_4) in biogas, which is taken as 50143 kJ/kg [43]. h_{air} and h_{comp} denote the specific enthalpy of air and other components in biogas, while $\dot{m}_{air}$, $\dot{m}_{meth}$ and $\dot{m}_{comp}$ represent the mass flow rates of air, methane, and other biogas components, respectively. The volume and mass fraction of each biogas component are listed in Table 1. To ensure complete combustion of the fuel, an excess air coefficient of 1.2 is applied.

The enthalpy of the hot flue gas within the CC can be expressed as (assume full combustion of the fuel in the CC):

$$\dot{H}_{HG} = \dot{m}_{HG} c_{p,HG} T_{HG} = \left(\dot{m}_{fuel} + \dot{m}_{air} \right) c_{p,HG} T_{HG} \tag{13}$$

where $\dot{m}_{HG}$, $c_{p,HG}$, and T_{HG} represent the mass flow rate, specific heat at constant pressure, and temperature of the hot flue gas, respectively.

In Eq. (10), the total heat transferred from the hot flue gas in the CC to the Stirling engine heater can be divided into convective heat transfer and radiative heat transfer:

$$\dot{Q}_{h,ac} = \dot{Q}_{conv} + \dot{Q}_{radi} \tag{14}$$

where the convective and radiative heat transfer between the flue gas and the heater are represented as:

$$\dot{Q}_{conv} = h_{HO} A_{HO} (T_{HG} - T_H) \tag{15}$$

$$\dot{Q}_{radi} = \varepsilon A_{HO} \sigma_0 \left(T_{HG}^4 - T_H^4 \right) \tag{16}$$

where ε represents the emissivity, which is assumed to be 1 in this study. σ_0 is the Stefan-Boltzmann coefficient. h_{HO} denotes the convective heat transfer coefficient between the flue gas and the heater tube wall, and it can be determined using empirical formulas dependent on the Reynolds number. A_{HO} represents the outer surface area of the heater tube wall and can be obtained using the following equation:

$$A_{HO} = \pi N_H L_H D_{HO} \tag{17}$$

where N_H, L_H, and D_{HO} denote the number, length, and outer diameter of the heater tubes, respectively. By simultaneously solving Eqs. (10)-(16), the mass flow rate of the fuel $\dot{m}_{fuel}$ and temperature of the hot flue gas (T_{HG}) in the CC can be determined.

2.4. Heating boiler subsystem modeling

In the CHP system, obtaining the water inlet temperature ($T_{w,i}$) is usually straightforward, whereas the temperature of the Stirling engine cooler wall (T_K) is influenced by various operational and geometrical parameters within the system. Therefore, the water inlet temperature ($T_{w,i}$) and mass flow rate ($\dot{m}_w$) are specified, and the cooler wall temperature is initialized to the water inlet temperature, i.e., $T_K^0 = T_{w,i}$. Before solving the energy balance equation for the HB subsystem, it is necessary to determine the temperature of water entering the HB ($T_{w,md}$). $T_{w,md}$ can be obtained from the energy balance equation for the

Table 1
Volume and mass fractions of various components for biogas [44].

Component	Methane (CH_4)	Carbon dioxide (CO_2)	Water (H_2O)	Hydrogen sulfide (H_2S)
Volume fraction	60.0 %	38.0 %	2.0 %	100.0 ppm
Mass fraction	36.0 %	62.7 %	1.3 %	0 %

cooler:

$$\dot{Q}_{k,ac} = -\dot{m}_w c_{p,w}\left(T_{w,md} - T_{w,i}\right) \tag{18}$$

where $c_{p,w}$ represents the specific heat at constant pressure of water.

In the above equation, the heat transfer of the cooler ($\dot{Q}_{k,ac}$) is calculated based on the initial cooler wall temperature (T_K^0), which introduces a certain deviation from the actual value. To obtain a more accurate heat transfer for the cooler, it is essential to correct the cooler wall temperature accordingly. For the cooler, the following thermal energy transfer equation can be applied to its outer surface:

$$\dot{Q}_{k,ac} = h_{KO} A_{KO}\left(T_K - T_{w,mK}\right) \tag{19}$$

where $T_{w,mK}$ represents the average temperature of water inside the cooler, calculated as $T_{w,mK} = \left(T_{w,i} + T_{w,md}\right)/2$. h_{KO} denotes the convective heat transfer coefficient between water and the outer surface of the cooler tube, similarly obtained from empirical formulas based on the Reynolds number. A_{KO} stands for the outer surface area of the cooler tube, which can be determined using the following expression:

$$A_{KO} = \pi N_K L_K D_{KO} \tag{20}$$

where N_K, L_K, and D_{KO} represent the number, length, and outer diameter of the cooler tube, respectively.

Combining Eqs. (18) and (19), the cooler wall temperature T_K can be iteratively corrected, thereby obtaining accurate values of $\dot{Q}_{k,ac}$ and $T_{w,md}$.

Next, the energy equations for the water side and the flue gas side of the HB subsystem are formulated separately:

$$\dot{Q}_{hb} = \dot{H}_{w,o} - \dot{H}_{w,md} = \dot{m}_w c_{p,w}\left(T_{w,o} - T_{w,md}\right) \tag{21}$$

$$\dot{Q}_{hb} = \dot{H}_{HG} - \dot{H}_{exh} = \dot{m}_{HG} c_{p,HG} T_{HG} - \dot{m}_{HG} c_{p,exh} T_{exh} \tag{22}$$

where $\dot{H}_{w,o}$ and $\dot{H}_{w,md}$ stand for the enthalpy of the water in the outlet and entering the HB, respectively. $T_{w,o}$ represents the water outlet temperature, while $c_{p,exh}$ and T_{exh} denote the specific heat at constant pressure and temperature of the exhaust gas at the outlet of the HB, respectively.

Additionally, there is the thermal energy transfer equation:

$$\dot{Q}_{hb} = h_{hb} A_{hbo} \Delta T_{exhw,m} = h_{hb} A_{hbo} \frac{\left(T_{HG} - T_{w,o}\right) - \left(T_{exh} - T_{w,md}\right)}{\ln\left(\left(T_{HG} - T_{w,o}\right)/\left(T_{exh} - T_{w,md}\right)\right)} \tag{23}$$

where $\Delta T_{exhw,m}$ represents the logarithmic mean temperature difference between the flue gas and water. h_{hb} denotes the overall heat transfer coefficient between the flue gas and water inside the HB, and A_{hbo} is the outer surface area of the tube wall, calculated by the following two equations:

$$h_{hb} = \frac{1}{\frac{D_{hbo}}{D_{hbi} h_{hbi}} + \frac{1}{h_{hbo}}} \tag{24}$$

$$A_{hbo} = \pi N_{hb} L_{hb} D_{hbo} \tag{25}$$

where N_{hb}, L_{hb}, D_{hbo}, and D_{hbi} represent the number, length, outer diameter, and inner diameter of the water tubes inside the HB, respectively. Meanwhile, h_{hbo} and h_{hbi} denote the heat transfer coefficient on the outer and inner surfaces of the water tubes, respectively, which are determined using empirical formulas based on their respective Reynolds numbers.

The Reynolds numbers of the working fluids inside and outside the water tubes are calculated as follows:

$$Re_{hbi} = \frac{\dot{m}_w D_{hbi}}{A_{s,hbi} \mu_w} = \frac{4\dot{m}_w}{\pi D_{hbi} \mu_w} \tag{26}$$

$$Re_{hbo} = \frac{\dot{m}_{HG} D_{hbo}}{A_{s,hbo} \mu_{exh,m}} \tag{27}$$

where $\mu_{exh,m}$ represents the average viscosity of the flue gas inside the HB. $A_{s,hbi}$ and $A_{s,hbo}$ respectively denote the average flow cross-sectional areas of the working fluid inside and outside the water tubes in the HB, where $A_{s,hbo}$ is calculated as:

$$A_{s,hbo} = \frac{L_{hb} W_{hb}}{N_{hbexh} + 1} \tag{28}$$

where W_{hb} represents the width of the HB, and N_{hbexh} denotes the number of baffles on the shell side.

By simultaneously solving Eqs. (21)–(23), the outlet temperature of flue gas (T_{exh}) and water ($T_{w,o}$) inside the HB can be obtained, thereby determining the heat transfer between the flue gas and water within the HB ($\dot{Q}_{hb}$).

Additionally, within the CHP system, a portion of the electrical power output is consumed by the water pump to drive the circulation of water within the system. The power consumption of the water pump during its operation is given by:

$$P_{hb,loss} = \Delta p_{w,hbi} \frac{\dot{m}_w}{\rho_w} \tag{29}$$

where $\Delta p_{w,hbi}$ denotes the pressure drop within the water tubes of the HB.

2.5. Comprehensive performance evaluation of micro combined heat and power systems

Based on the aforementioned three submodels, the actual electrical power output of the Stirling engine-based micro-CHP system is:

$$P_{el} = P_{ac} - P_{hb,loss} \tag{30}$$

Therefore, the electrical efficiency of the system is:

$$\eta_{el} = \frac{P_{el}}{\dot{H}_{fuel}} \tag{31}$$

The heat output efficiency and overall efficiency of the system are:

$$\eta_{he} = \frac{-\dot{Q}_{k,ac} + \dot{Q}_{hb}}{\dot{H}_{fuel}} \tag{32}$$

$$\eta_{to} = \eta_{el} + \eta_{he} \tag{33}$$

However, the above overall efficiency only considers the comprehensive effectiveness of energy utilization within the system, disregarding the magnitude of the building's electrical power demand. This may result in insufficient electrical power output. Besides ensuring reasonable energy utilization efficiency, achieving higher electrical power output is equally crucial for CHP systems. By factoring in electrical power output into the comprehensive performance evaluation, the system could potentially achieve higher electrical power output, thus aiding in meeting the larger peak electricity demands of buildings, even though this may require more fuel supply. However, the surplus heat is not wasted but efficiently utilized in hot water production. Therefore, to more effectively characterize the comprehensive thermal-electric performance of the CHP system, a dimensionless performance index F that simultaneously considers the system's electrical power and heat output efficiency is defined based on specific performance base values:

$$F = \left(\frac{P_{el}}{1 - \eta_{he}} \Big/ \frac{P_{el,base}}{1 - \eta_{he,base}} + \frac{\eta_{he}}{\eta_{he,base}}\right)/2 \tag{34}$$

where the subscript "base" denotes the performance of the CHP system

under specific geometries chosen as a base point. It is noted that the value of F represents the arithmetic mean of the improvement percentage in both electrical output and heat output performance relative to the base value. When there is an overall performance improvement, F exceeds 1; conversely, when there is an overall performance decline, F is less than 1.

2.6. Constructal optimization strategies

This study, based on constructal theory, employs the new model of Stirling engine-based micro-CHP systems to perform geometric optimization of crucial thermal energy transfer components within the system, aiming to explore avenues for enhancing the system's overall thermal-electric performance. Constructal optimization typically focuses on the evolution of local dimensions under reasonable global geometric constraints to achieve optimal system performance [36]. Herein, the global geometric constraints and coordinated optimization strategies of the significant local geometric parameters for thermal energy transfer components are presented.

(1) Regenerator

The dead volume and matrix volume of the regenerator are vital for its heat and mass transfer performance. To ensure that changes in volume do not obscure the impact of local geometry on system performance, the total volume of the regenerator is maintained constant:

$$V_{rt} = \frac{\pi}{4}\left(D_{RO}^2 - D_{RI}^2\right)L_R = \text{Constant} \tag{35}$$

where L_R, D_{RO}, and D_{RI} represent the length, outer diameter, and inner diameter of the regenerator, respectively.

Additionally, constrained by the cylinder diameter of the Stirling engine, the inner diameter of the regenerator remains constant. Therefore, the local dimensions of the regenerator will vary together under a single degree of freedom, with this study focusing on the regenerator length (L_R) as the primary research variable. Furthermore, the porosity of the regenerator significantly influences the interaction between the gas and the matrix. Hence, the porosity (φ) is considered as the secondary research variable.

(2) Heater

The dead volume within the heater significantly impacts system performance. To highlight the role of local geometric construction, the total dead volume within the heater is kept constant:

$$V_h = \frac{\pi}{4}N_H L_H D_h^2 = \text{Constant} \tag{36}$$

The equation above indicates that variations in the local geometric parameters of the heater possess dual degrees of freedom. Therefore, the primary research variable chosen here is the length of the heater tube (L_H), while the number of heater tubes (N_H) serves as the secondary research variable.

(3) Cooler

Similar to the heater, the total dead volume of the cooler is kept constant.

$$V_k = \frac{\pi}{4}N_K L_K D_k^2 = \text{Constant} \tag{37}$$

Likewise, changes in the local geometric parameters of the cooler also exhibit dual degrees of freedom. Herein, the length of the cooler tube (L_K) is selected as the primary research variable, while the number of cooler tubes (N_K) serves as the secondary research variable.

(4) Heating boiler

Typically, the global dimensions of the heating boiler are constrained by limited installation space. Here, the length (L_{hb}) and width (W_{hb}) of the heating boiler are maintained constant. Additionally, to ensure consistent heat exchange time for water within the heating boiler at the same flow rate, the internal volume of the water tubes remains constant. Consequently, the geometry of the heating boiler is governed by the following constraints:

$$L_{hb}, W_{hb} = \text{Constant} \tag{38}$$

$$V_{hbi} = \frac{\pi}{4}N_{hb}L_{hb}D_{hbi}^2 = \text{Constant} \tag{39}$$

In Eq. (39), the local geometric parameters of the heating boiler experience coordinated variations under a single degree of freedom, with the number of water tubes (N_{hb}) chosen as the primary research variable. Moreover, the number of baffles (N_{hbexh}) inside the heating boiler notably impacts the flow of flue gas outside the tubes, thus serving as the secondary research variable.

2.7. Model solution methods

In this study, a Matlab code for numerically solving the Stirling engine-based micro-CHP system model has been developed. The algorithmic flowchart of the code is depicted in Fig. 4. Initially, the essential geometric dimensions of various components within the micro-CHP system, along with specified operational parameters such as the Stirling engine's hot-end temperature (T_H), water mass flow rate ($\dot{m}_w$), and water inlet temperature ($T_{w,i}$), need to be input. Subsequently, the Stirling engine's cold-end temperature (T_K) is initialized to the water inlet temperature. Based on these known geometric and operational parameters, the temperature, pressure, mass, and polytropic index of the secondary components within the SPEC model (SE-G submodel) are initialized. Following this, the SPEC model is iteratively solved using the fourth-order Runge-Kutta (RK-4) method and the determined initial values until the physical fields within the Stirling engine reach a state of periodic stability, indicating convergence of the submodel calculation.

Once the SPEC model converges, the ideal output performance and various energy losses of the SE-G subsystem are computed based on the steady physical fields of the SE. This further yields modified electrical

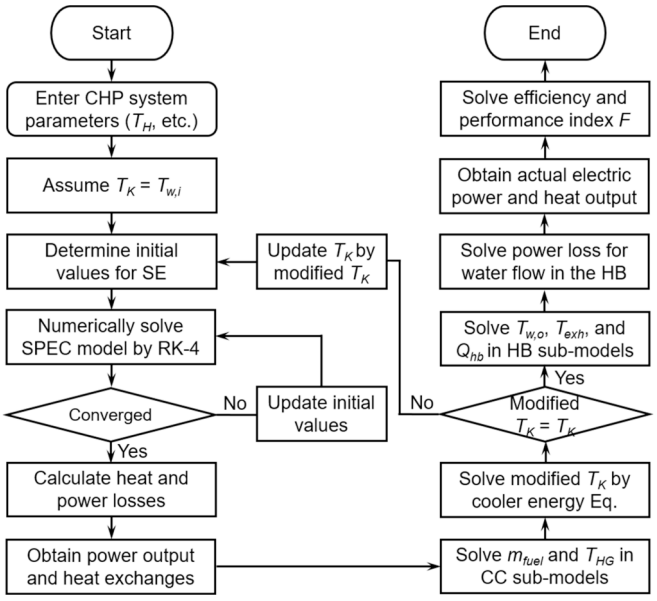

Fig. 4. Algorithmic flowchart of the current micro-CHP system model.

power output and heat transfer rates. Subsequently, the heat absorption rate ($\dot{Q}_{h,ac}$) and heat release rate ($\dot{Q}_{k,ac}$) obtained from the SE-G submodel are respectively input into the CC and HB submodels to determine the system's gas mass flow rate ($\dot{m}_{fuel}$), hot flue gas temperature (T_{HG}), and modified cooler wall temperature (T_K). If the modified value of T_K differs from its initial value, the initial value of T_K is replaced with the new modified value, and the three submodels are re-solved until the new modified value of T_K equals the original value.

When the calculation of T_K converges, the modified $\dot{Q}_{k,ac}$ and T_{HG} of the SE are input into the HB submodel to solve for the water temperature ($T_{w,o}$) and the exhaust gas temperature (T_{exh}) at the HB outlet. Subsequently, the heat transfer rate between water and flue gas ($\dot{Q}_{hb}$), as well as the pump power consumed by water flow ($P_{hb,loss}$) inside the HB tubes, is calculated. Finally, based on the obtained SE-G electrical power output, pump power consumption, and water-flue gas heat exchange, the actual electrical power and heat output performance of the micro-CHP system are determined, resulting in the comprehensive performance index F value.

3. Results and discussion

This section first discusses the accuracy of the micro-CHP system model. Then, constructal optimization of the key thermal energy transfer components within the system is performed, and the overall thermal-electric performance, as well as the critical parameter combinations before and after optimization, are compared.

3.1. Validation of the micro combined heat and power system model

The heat-to-power conversion processes within the CHP system occur exclusively within the SE-G subsystem, while only thermal energy transfer processes exist within the CC and HB subsystems. In the present model, the predictive formulas for the performance of thermal energy transfer processes primarily stem from theoretical derivations and experimental data fitting found in the public literature, whose efficacy has been thoroughly validated through long-term engineering practice. Therefore, this study does not further validate the accuracy of modeling the CC and HB subsystems. Instead, only the new SE-G submodel is evaluated to verify its accuracy in predicting the critical heat-to-power conversion performance of the system.

The GPU-3 β-type Stirling engine, manufactured by General Motors [45], is extensively employed for validating Stirling thermal models. In this study, the geometric and operational parameters of this engine are integrated into the present SPEC model to assess its performance. The primary specifications of the GPU-3 Stirling engine are summarized in Table S1 in Supplementary Material. The engine's output power and thermal efficiency predicted by the present model are compared with experimental data from NASA Lewis Research Center [45], along with numerical results from other thermal models such as Simple (Urieli et al. [33]), Simple II (Babaelahi et al. [46]), Combined Adiabatic-Finite Speed thermal model (CAFS, Hosseinzade et al. [47]), Polytropic-Finite Speed thermodynamics (PFST, Hosseinzade et al. [48]), Polytropic Analysis of Stirling Engine with Various Losses (PSVL, Babaelahi et al. [34]), Polytropic Stirling Model with Losses (PSML, Li et al. [49]), and Modified Non-ideal thermal model of Stirling Engines with Various Losses (MSVL, Udeh et al. [50]).

Fig. 5 depicts the comparison between the output power and thermal efficiency predicted by the present model and other thermal models, against experimental values, at different engine speeds with a heat source temperature of 922 K, a heat sink temperature of 286 K, and an average pressure of 4.14 MPa. It is evident that across the engine speeds within the entire investigated range, the present model accurately predicts both output power and thermal efficiency, showing good agreement with experimental values and demonstrating consistent trends. As illustrated in Fig. 5(a), compared to other thermal models, the accuracy

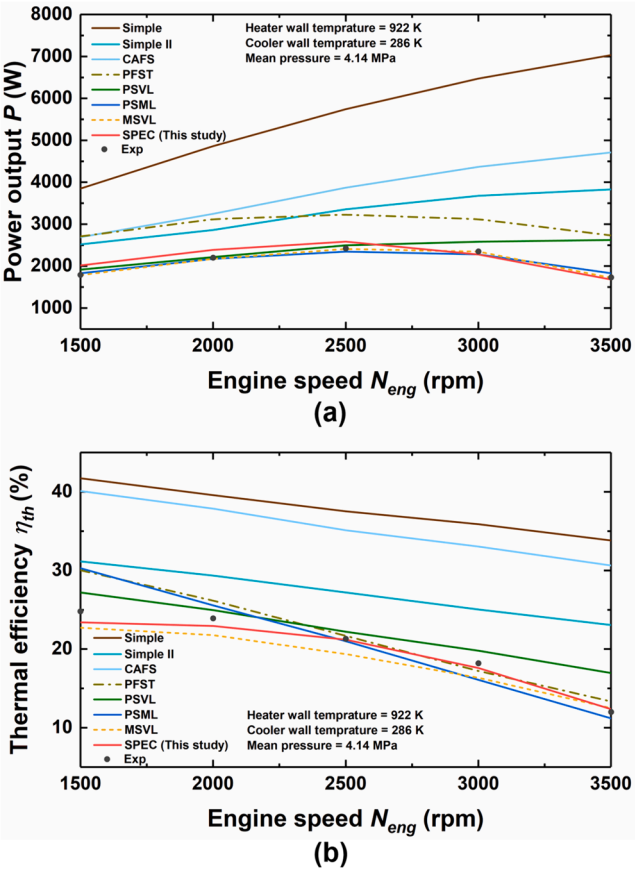

Fig. 5. Comparison between the output power and thermal efficiency predicted by the SPEC model and other thermal models, against experimental values at different engine speeds under an average pressure of 4.14 MPa.

of output power predicted by the present model significantly surpasses that of the Simple, Simple II, CAFS, and PFST, approaching the level of PSML and MSVL models. However, at low engine speeds, the present model predicts slightly higher deviations in output power compared to the PSML and MSVL models. This discrepancy may stem from the omission of power losses caused by gas leakage from the expansion chamber to the compressor chamber through the clearance between the displacer and the cylinder wall in the present model. As the engine speed increases, power losses attributed to heat exchanger pressure drop, mechanical friction, limited piston motion, and gas spring hysteresis escalate rapidly, resulting in a decrease in the proportion of working chamber gas leakage losses to total power losses, thereby enhancing the accuracy of the present model.

Additionally, as depicted in Fig. 5(b), the present model exhibits the highest level of accuracy in predicting thermal efficiency across all speeds. This is because the original differential equation derivation of the current model not only incorporates the effects of irreversible factors such as heat exchanger pressure drop and imperfect regeneration, which are typically not addressed in most thermal models, on the transient physical field distribution and its variation in components, but also synchronously considers changes in engine operational characteristics due to polytropic compression/expansion and endothermic/exothermic processes. Consequently, the present model can more accurately predict the heat transfer between the Stirling engine and external heat sources/sinks through the heater/cooler, resulting in more accurate engine thermal efficiency values.

When the average pressure of the gas within the Stirling engine decreases, it leads to variations in the predictive accuracy of different thermal models for engine performance. Fig. 6 presents a comparison between the output power and thermal efficiency calculated by the

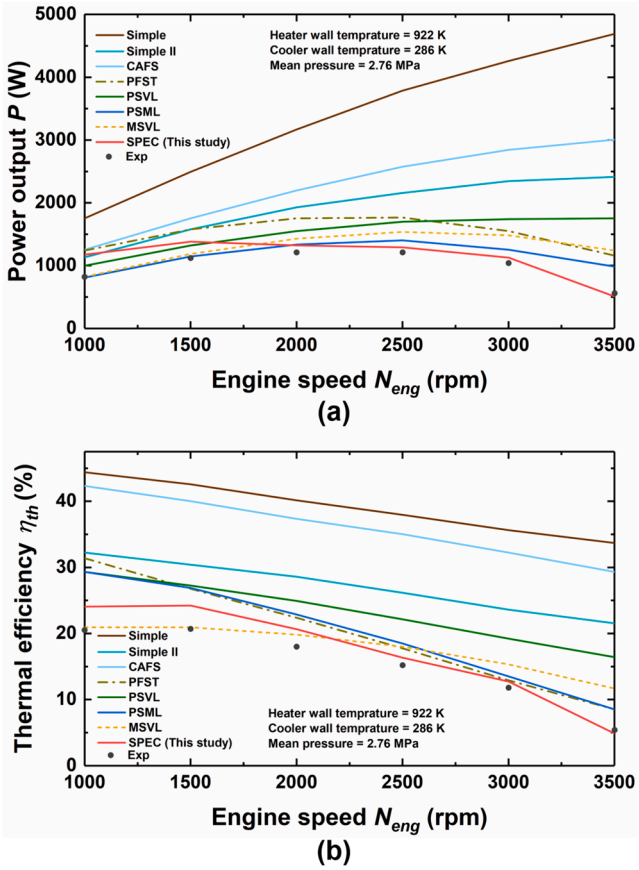

Fig. 6. Comparison between the output power and thermal efficiency predicted by the SPEC model and other thermal models, against experimental values at different engine speeds under an average pressure of 2.76 MPa.

present model and other thermal models against experimental values within the range of engine speeds studied, with a heat source temperature of 922 K, a heat sink temperature of 286 K, and an average pressure of 2.76 MPa. As depicted in Fig. 6(a), the present model consistently reproduces output power trends that align with experimental values. Across most speed ranges (N_{eng} = 2000–3500 rpm), the output power predicted by the current model closely aligns with experimental values, exhibiting only slightly higher deviations at lower speeds (N_{eng} < 2000 rpm). When the speed drops below 1500 rpm, the predictive accuracy of the present model is slightly lower than that of the PSVL, PSML, and MSVL models but higher than that of the Simple, Simple II, CAFS, and PFST models. Conversely, when the speed exceeds 2000 rpm, the predictive accuracy of the present model for engine output power surpasses that of all other thermal models. This is attributed to the more precise assumptions concerning polytropic working and heat transfer processes within the current model, as well as the correction of instantaneous pressure for each component.

In Fig. 6(b), the present model successfully predicts the trend of thermal efficiency, exhibiting a stable state with increasing speed (N_{eng} = 1000–1500 rpm) followed by a progressively intensified monotonic decrease (N_{eng} = 1500–3500 rpm). Similarly, at lower speeds, a slightly higher deviation in predicted output power leads to a marginally increase in the deviations of thermal efficiency relative to experimental values. However, as the speed increases, the predictive accuracy improves significantly. Additionally, at all speeds, the predictive accuracy of the SPEC model exceeds that of the Simple, Simple II, CAFS, PFST, PSVL, and PSML models, only falling behind the MSVL model when the speed is below 2000 rpm. However, as the speed exceeds 2000 rpm, the predictive accuracy of the present model for engine thermal efficiency surpasses that of the MSVL model. This is also attributed to the former's more precise assumptions regarding polytropic processes within the working chamber and heat exchanger, resulting in more accurate output power and heat absorption. Therefore, through the comprehensive comparison of the predicted results in Figs. 5 and 6, the proposed present model demonstrates a high level of accuracy in predicting the heat-to-power conversion performance of Stirling engines across a broader range of operational conditions.

3.2. Constructal optimization of key thermal energy transfer components in the system

Similarly, a case study on the micro-CHP system model is conducted based on the specifications of the GPU-3 β-type Stirling engine [45] to evaluate the model's feasibility in predicting and optimizing the comprehensive thermal-electric performance of the system. In the following, constructal optimization is performed on four crucial thermal energy transfer components within the system: the regenerator, heater, cooler, and heating boiler, and a comparison of the primary output performance of the system, along with their corresponding key geometric and operational parameters, is conducted before and after optimization.

3.2.1. Regenerator

Fig. 7 presents the variations in various thermal-electric performance criteria of the micro-CHP system with three different types of regenerators as a function of regenerator length (L_R). The comprehensive performance index F is calculated using the GPU-3 Stirling engine's original cross-flow regenerator with a porosity (φ) of 0.7 and a length of 22.6 mm as the base structure. At this point, the micro-CHP system yields an electrical power output (P_{el}) of 2584 W, with heat output and overall efficiency (η_{he} and η_{to}) of 77.8 % and 87.2 %, respectively. It is evident that with increasing regenerator length, the electrical power output of the micro-CHP system decreases due to amplified pressure drop losses within the regenerator. However, the impact of regenerator length variations on the comprehensive thermal-electric performance index F varies among the three types of regenerators. Within the micro-CHP system, besides the fraction of heat converted into electrical power and power losses, the remaining heat generated by the fuel dissipates through water and exhaust gas. As the regenerator length changes, the Stirling engine's ideal work remains constant, implying the sum of electrical power and power losses remains constant. At this stage, the system's heat output performance is primarily influenced by the proportion of heat carried away by the exhaust gas, contingent upon the effectiveness of heat transfer between water and exhaust gas in the HB.

Specifically, in the case of the cross-flow regenerator, its high regeneration effectiveness leads to reduced heat absorption requirements by the Stirling engine, resulting in a smaller fuel mass flow rate. Consequently, the flue gas velocity within the HB is low, facilitating sufficient time for heat transfer between the flue gas and water. At this moment, the effectiveness of heat transfer between gas and water is primarily determined by the intensity of heat transfer. With an increase in regenerator length, the regeneration effectiveness continues to rise, further lowering the mass flow rate of flue gas and diminishing the heat transfer intensity within the HB. As a result, the effectiveness of heat transfer between water and exhaust gas declines, leading to a decrease in the system's heat output efficiency. Coupled with the reduction in electrical power output, this results in a declining trend in the comprehensive performance index F of the system. In contrast, for the parallel-flow regenerator, its regeneration effectiveness is low, necessitating higher heat absorption requirements and significantly increasing the mass flow rate and velocity of flue gas within the HB. Consequently, the heat transfer time between flue gas and water is insufficient. However, as the regenerator length increases, the regeneration effectiveness improves, leading to a decrease in the flow velocity of flue gas within the HB and a significant increase in heat transfer time. Consequently, the heat output efficiency of the system increases. With the parallel-flow

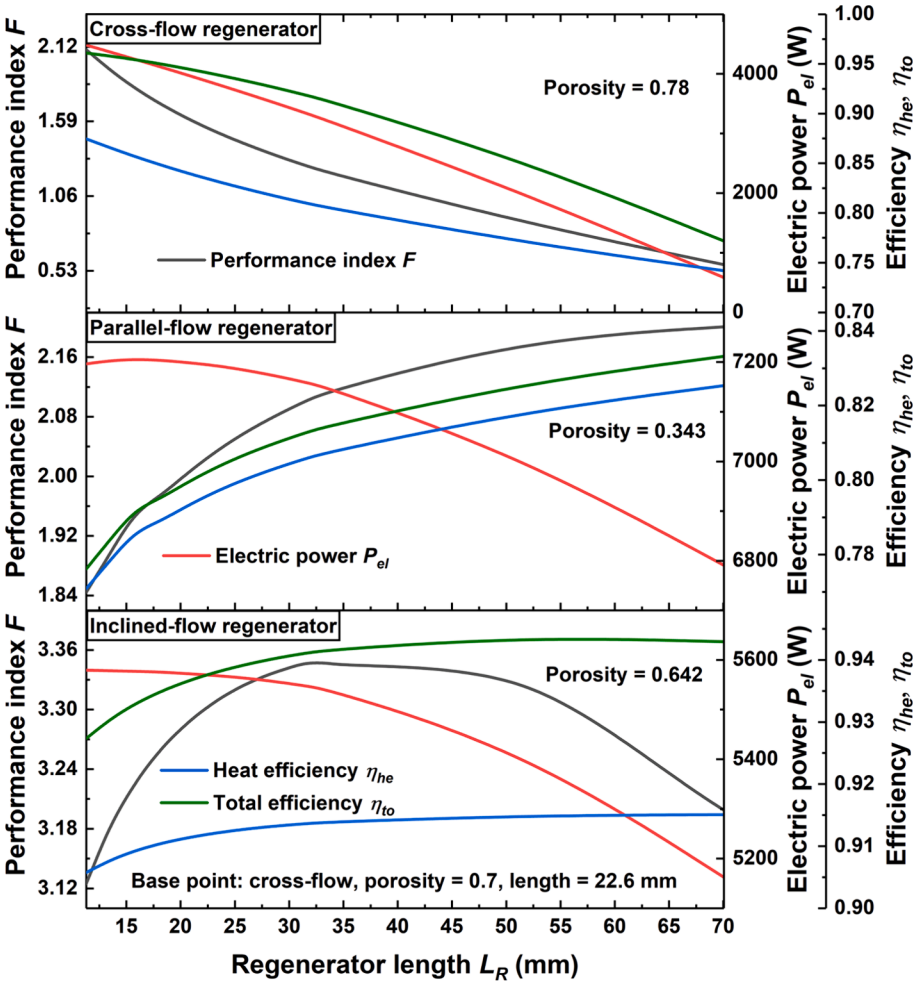

Fig. 7. Variations in various thermal-electric performance criteria of the micro-CHP system with three different types of regenerators as a function of regenerator length.

regenerator's characteristic of low pressure drop, an increase in regenerator length results in a limited increase in power losses, leading to a slower change in electrical power output. Consequently, the comprehensive performance index F is primarily influenced by changes in heat output efficiency, exhibiting an increasing trend with the increase in regenerator length. On the other hand, the inclined-flow regenerator exhibits moderate regenerative effectiveness, requiring a moderate fuel mass flow rate. At this point, the heat transfer time between flue gas and

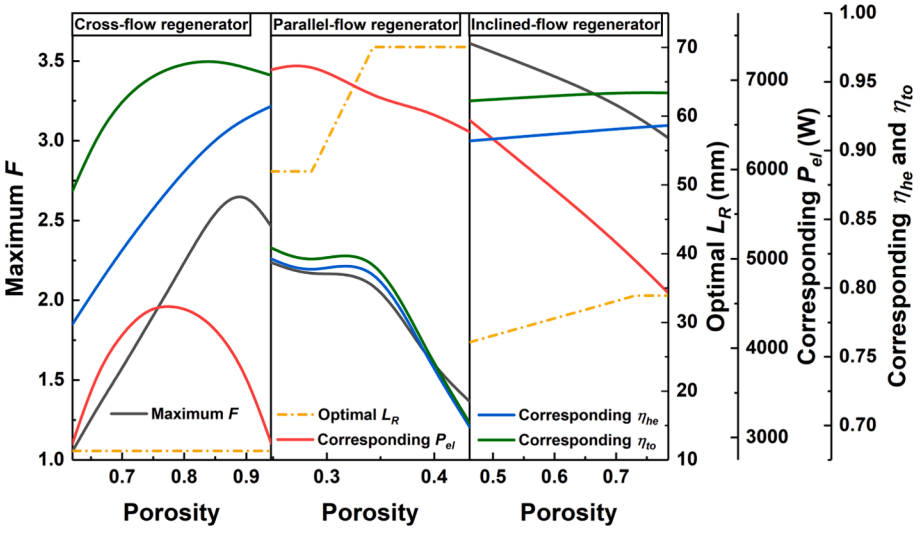

Fig. 8. Maximum comprehensive performance index F of the micro-CHP system under optimal regenerator length for three different types of regenerators across various porosities, along with corresponding values of other performance criteria.

water is slightly insufficient, and the heat transfer between the two working fluids is influenced by both heat transfer time and intensity. With an increase in regenerator length, the regeneration effectiveness rises, the flue gas velocity within the HB decreases, and the heat transfer time between flue gas and water lengthens, resulting in a gradual increase in heat output efficiency. However, as the regenerator length further increases, the impact of the reduced heat transfer intensity due to decreased flue gas velocity gradually becomes significant, offsetting the increase in heat output efficiency. As a result, the variation in heat output efficiency stabilizes. Due to the varying magnitude of changes in electrical power and heat output efficiency across different regenerator length ranges, the comprehensive performance index F shows a trend of increasing and then decreasing with increasing regenerator length.

Fig. 8 illustrates the maximum comprehensive performance index F of the micro-CHP system under optimal regenerator length (L_R) for three different types of regenerators across various porosities (φ), along with corresponding values of other performance criteria. The porosity for each type of regenerator is selected within a practical application range suitable for its specific structure. For the cross-flow regenerator, increasing porosity results in an expansion of the regenerator's dead volume, leading to a decline in the system's ideal electrical power output. However, the notable decrease in flow resistance within the regenerator causes a substantial reduction in power losses, which in turn results in an increase in the actual electrical power output. Nonetheless, with further increases in porosity, the decrease in power losses due to regenerator flow resistance becomes limited, causing the actual electrical power output to diminish as the ideal power decreases. Furthermore, higher porosity leads to reduced regeneration effectiveness, increased mass flow rate and velocity of flue gas within the HB, intensified heat transfer between flue gas and water, thereby reducing the proportion of heat carried away by exhaust gas. Together with the decline in ideal power output, this leads to a significant rise in the proportion of heat carried away by water, thereby substantially boosting the system's heat output efficiency. Consequently, the maximum comprehensive performance index F experiences a significant initial increase due to the simultaneous rise in electrical power output and heat output efficiency, followed by a reversal attributed to the substantial decrease in electrical power output. For the parallel-flow regenerator, lower flow resistance and power loss proportions result in a monotonic decrease in actual electrical power output with decreasing ideal power as porosity increases. Additionally, increased porosity leads to a notable rise in flue gas velocity, causing a significant reduction in heat transfer time between flue gas and water. Consequently, flue gas–water heat transfer becomes increasingly inadequate, resulting in an overall decline in the system's heat output efficiency. Thus, the maximum comprehensive performance index F decreases monotonically with the concurrent decrease in electrical power and heat output efficiency. In the case of the inclined-flow regenerator, increasing porosity similarly leads to a monotonic decrease in actual electrical power output due to the reduced proportion of pressure drop losses within the regenerator. Moreover, the effects of changes in heat transfer time and intensity within the HB caused by increasing porosity approximately cancel out, resulting in only a slight overall increase in the system's heat output efficiency. Dominated by the decreasing trend in electrical power output, the maximum comprehensive performance index F decreases with increasing porosity for this type of regenerator. Additionally, the comparison across all three types of regenerators reveals that the maximum comprehensive performance index F exhibits partially or completely different trends from the corresponding system's total efficiency, emphasizing the importance of F in providing a comprehensive assessment of both electrical and thermal performance. This underscores the necessity of the defined comprehensive performance index F in this study.

On the other hand, through comparing the trends of the maximum thermal-electric performance index F and the corresponding optimal regenerator length (L_R) under varying porosities for the three types of regenerators, it can be generally inferred that the optimal regenerator length ranges for cross-flow, parallel-flow, and inclined-flow regenerators are relatively low, high, and moderate, respectively, while the optimal porosity ranges are high for the former and low for the latter two. This offers some degree of guidance for the optimization design of different types of regenerators. Additionally, when comparing the maximum thermal-electric performance index F values of micro-CHP systems under the three types of regenerators, the system equipped with a cross-flow regenerator shows low electrical power output and moderate heat output efficiency, whereas the system equipped with a parallel-flow regenerator exhibits high electrical power output and relatively low heat output efficiency. Therefore, the two types of regenerators generally demonstrate similar comprehensive thermal-electric performance. In contrast to the former two types of regenerators, the inclined-flow regenerator enables the system to achieve moderate electrical power output and higher heat output efficiency, ultimately demonstrating the highest comprehensive thermal-electric performance. This highlights the potential of the inclined-flow regenerator in enhancing the performance of SE-based micro-CHP systems. Consequently, in subsequent constructal optimizations, an inclined-flow regenerator with a length of 27.1 mm and a porosity of 0.462, yielding a dual maximum performance index F, is selected as the default regenerator structure.

3.2.2. Heater

Fig. 9 depicts the variation of the comprehensive performance index F and other performance criteria of the micro-CHP system with the number of heater tubes. The base structure of the heater with a tube length (L_H) of 245.3 mm and a number of heater tubes (N_H) of 40 is chosen for the calculation of F values. With an increase in the number of heater tubes, their diameter decreases, resulting in heightened flow resistance as the working gas traverses the tubes. Consequently, there's a marginal reduction in electrical power output. Additionally, the decreased tube diameter enhances the heat transfer area and intensity between the hot flue gas within the CC and the working gas inside the heater tubes, thereby improving the heat transfer performance between the two, and reducing the required fuel mass flow rate within the CC. Consequently, the flow velocity of flue gas inside the HB significantly decreases, weakening the heat transfer intensity between the flue gas and water but considerably extending the heat transfer time, leading to an increase in heat output efficiency. However, with further increases in the number of heater tubes, the heat transfer time between the flue gas and water becomes sufficient, and the effect of diminishing heat transfer intensity gradually becomes significant, resulting in a decelerated increase or even a slight decrease in heat output efficiency. The trend of the comprehensive performance index F with the number of heater tubes is successively dominated by the increase in heat output efficiency and the decrease in electrical power output, thus exhibiting an initial increase followed by a decrease. However, it's notable that the system's overall efficiency monotonically increases with the augmentation in the number of heater tubes, indicating its failure to accurately portray the comprehensive thermal-electric performance of the system and effectively determine the optimal geometric structure.

Fig. 10 illustrates the variation in the maximum comprehensive performance index F and other performance criteria of the system with the tube length of the heater (L_H) under the optimal number of heater tubes (N_H). As the tube length varies, the optimal number of heater tubes corresponding to the maximum comprehensive thermal-electric performance changes almost inversely. At this point, the diameter and total surface area of the heater tubes remain roughly constant, thereby maintaining relatively consistent heat transfer performance between the hot flue gas within the CC and the working gas inside the tubes. Consequently, the variation in required fuel mass flow rate is minimal, and the heat output performance tends to stabilize. However, longer tube length results in increased flow distance for the working gas inside the tubes, leading to greater power losses and a reduction in actual

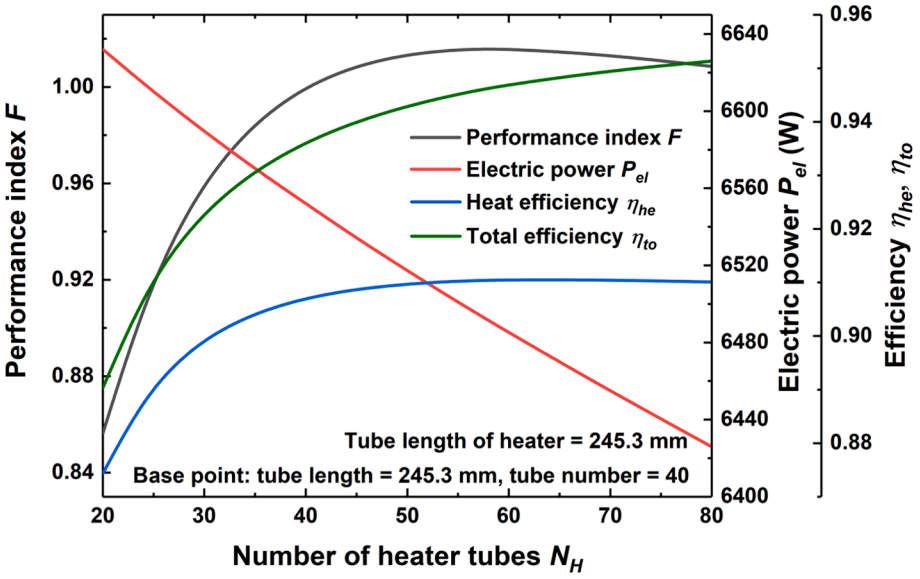

Fig. 9. Variation of the comprehensive performance index F and other performance criteria of the micro-CHP system with the number of heater tubes.

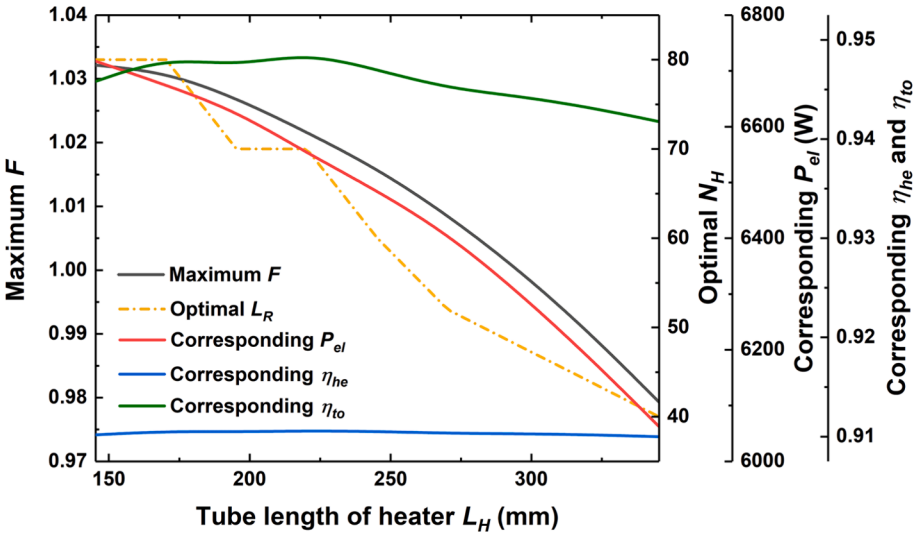

Fig. 10. Variation in the maximum comprehensive performance index F and other performance criteria of the system with the tube length of the heater under the optimal number of heater tubes.

electrical power output. Therefore, the maximum comprehensive performance index F decreases monotonically with the decrease in electrical power output. Building on this, a heater with a heater tube number of 80 and a length of 145.3 mm is adopted, corresponding to the dual maximum performance index F value, as the optimal geometric structure, which will be employed in subsequent constructal optimizations.

3.2.3. Cooler

Figs. 11 and 12 display the outcomes of the constructal optimization for the number and length of cooler tubes, respectively. Here, the base structure of the cooler for calculating the performance index F consists of cooler tubes with a length (L_K) of 46.1 mm and a number (N_K) of 312. A comprehensive observation from both figures reveals that augmenting the number and length of cooler tubes marginally reduces the electrical power output of the system, while exerting minimal influence on heat output efficiency, thus resulting in a slight decline in the overall thermal-electric performance of the system. This phenomenon arises due to the diminishing diameter of the cooler tubes as both the number and length of tubes increase, thereby elevating power losses resulting from the flow resistance of the working gas within the cooler tubes, consequently lowering electrical power output. Additionally, the heightened number and length of cooler tubes result in an expanded heat transfer surface area, enhancing the heat transfer performance between the working gas and water, thereby lowering the temperature of the cooler tube wall (T_K). However, the decline in T_K merely induces a slight upsurge in both the ideal output power and thermal efficiency of the Stirling engine, with minimal impact on the fuel demand within the CC and the heat transfer performance between the flue gas and water within the HB. As a result, the system's heat output efficiency remains nearly constant. Considering that a superior comprehensive thermal-electric performance index F can be attained with fewer cooler tubes and shorter tube length, a cooler comprising 132 tubes with a length of 26.1 mm is chosen as the optimal structure for subsequent constructal optimizations.

3.2.4. Heating boiler

Fig. 13 presents the impact of the number of water tubes (N_{hb}) inside the heating boiler (HB) on the comprehensive thermal-electric

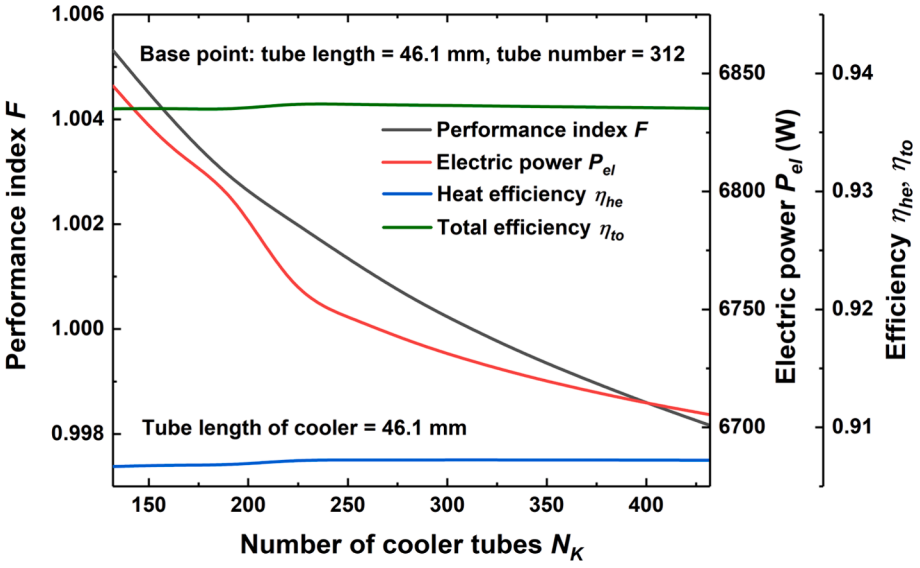

Fig. 11. Variation of the comprehensive performance index F and other performance criteria of the micro-CHP system with the number of cooler tubes.

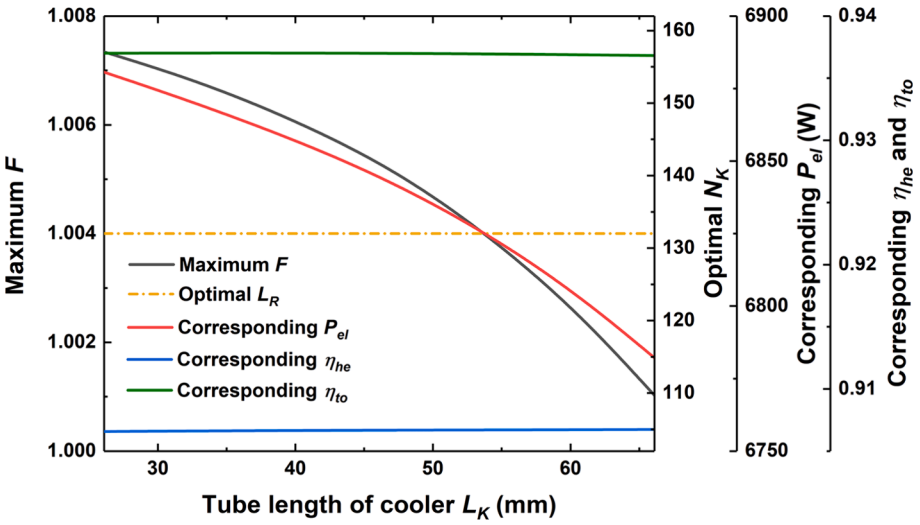

Fig. 12. Variation in the maximum comprehensive performance index F and other performance criteria of the system with the tube length of the cooler under the optimal number of cooler tubes.

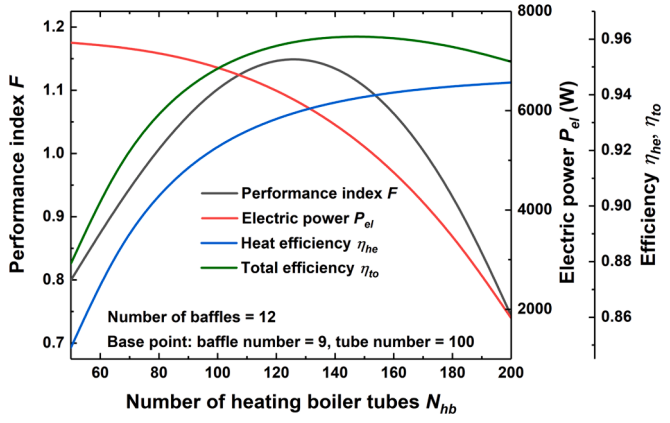

Fig. 13. Impact of the number of water tubes inside the heating boiler on the comprehensive thermal-electric performance index F and other key performance criteria of the micro-CHP system.

performance index F and other key performance criteria of the micro-CHP system. The base configuration of the HB for determining the F value consists of 9 baffles and 100 water tubes. As the number of water tubes increases, the total length of the tubes increases while the diameter of each tube gradually decreases. Consequently, the pressure losses incurred as water flows through the tubes rapidly escalate, causing a substantial increase in the electrical power consumption required by the water pump to drive the flow, thus resulting in a notable decrease in the actual electrical power output of the system. Simultaneously, the increase in the number of water tubes leads to a decrease in tubes diameter, improves the heat transfer area and intensity between the flue gas and water inside the HB, thereby significantly enhancing the heat output efficiency. The comprehensive performance index F is successively influenced by the increase in heat output efficiency and the decrease in electrical power output, thereby exhibiting a trend of increase followed by decrease. Additionally, it appears that the system's overall efficiency also captures the decrease in its electrical output performance, thus demonstrating a similar trend to that of the performance index F, albeit with some differences in the magnitude of change.

Fig. 14 illustrates the variation of the maximum comprehensive

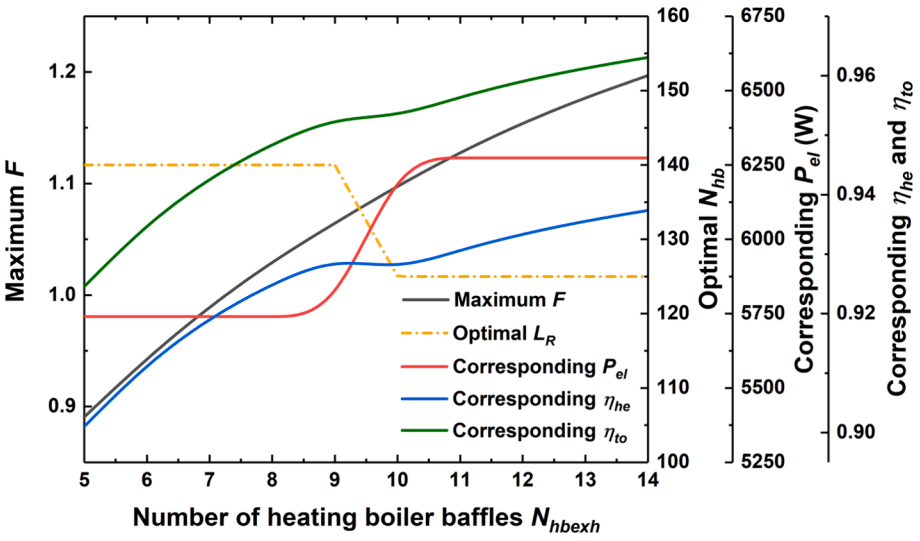

Fig. 14. Variation of the maximum comprehensive performance index *F* and other crucial performance criteria of the micro-CHP system with the number of baffles inside the HB, under the optimal number of water tubes.

performance index *F* and other crucial performance criteria of the micro-CHP system with the number of baffles (N_{hbexh}) inside the HB, under the optimal number of water tubes (N_{hb}). The change in the number of baffles itself has no impact on the electrical power output. However, an increase in the number of baffles correlates with a general downward trend in the optimal number of water tubes inside the HB, resulting in a gradual improvement in the system's electrical power output. On the other hand, the increase in the number of baffles diminishes the cross-sectional area for flue gas flow within the HB, thereby elevating the velocity of the flue gas. This augmentation intensifies the convective heat transfer between the flue gas and water, resulting in an enhanced heat output efficiency of the system. The simultaneous increase in electrical power and heat output efficiency contributes to a monotonically increasing trend in the maximum comprehensive performance index *F* with the increase in the number of baffles. Therefore, an HB with the optimal structure, corresponding to the dual maximum *F* value, is selected, comprising 125 water tubes and 14 baffles. Under this configuration, the system achieves optimal performance with an electrical power output (P_{el}) of 6274 W, a heat output efficiency (η_{he}) of 93.7 %, and a total efficiency (η_{to}) of 96.3 %. This high energy utilization efficiency falls within the typical range of maximum overall efficiency for existing Stirling engine-based CHP systems, generally ranging from 85 % to 97 % [1]. However, the inclined-flow regenerator utilized in this study provides balanced flow resistance and heat transfer characteristics, enabling the CHP system to achieve a higher electrical power output, albeit with a relatively lower electrical efficiency compared to systems equipped with cross-flow regenerators reported in the literature [1]. Consequently, the thermal efficiency of systems significantly surpasses that of other existing CHP systems, which typically range from 60 % to 82 % [1].

3.2.5. Comparison of performance before and after optimization

The preceding sections have sequentially conducted constructal optimizations on the pivotal thermal energy transfer components within the Stirling engine-based micro-CHP system: the regenerator, heater, cooler, and heating boiler, yielding the optimal geometric structures and output performance. In the following, a comparison of the key geometric and operational parameters, along with significant performance criteria, is presented before and after optimization, as depicted in Table 2.

Significant differences can be observed in the geometric structures of the thermal energy transfer components and operational parameters, such as supply water temperature and fuel mass flow rate, before and after optimization. Following optimization, the comprehensive thermal-electric performance index *F* of the system reaches 4.9. Furthermore, the electrical power output has increased by 142.8 %, while the heat output efficiency and total efficiency have increased by 20.5 % and 10.5 %, respectively. These results underscore the feasibility of the novel Stirling engine-based micro-CHP system model proposed in this study, as well as the efficacy of introducing constructal theory to predict and enhance the comprehensive thermal-electric performance of the system.

Table 2
Key geometric and operational parameters, along with crucial performance criteria of the Stirling engine-based micro-CHP system before and after optimization.

Specification	Before optimization	After optimization
Geometric parameter		
Regenerator type	Cross-flow	Inclined-flow
Regenerator porosity	0.7	0.462
Regenerator length	22.6 mm	27.1 mm
Heater tube number	40	80
Heater tube length	245.3 mm	145.3 mm
Cooler tube number	312	132
Cooler tube length	46.1 mm	26.1 mm
HB water tube number	100	125
HB baffle number	9	14
Operational parameter		
Water mass flow rate	60 L/min	60 L/min
Water inlet temperature	283 K	283 K
Water outlet temperature	293.8 K	337.5 K
Fuel mass flow rate	1.593 g/s	13.3 g/s
Hot flue gas temperature	1204.3 K	1544.8 K
Exhaust gas temperature	286.6 K	311.7 K
Performance criterion		
Electrical power output	2584 W	6274 W
Heat output efficiency	77.8 %	93.7 %
Total efficiency	87.2 %	96.3 %
Performance index *F*	1	4.9

4. Conclusion

This paper, based on a Stirling thermal analysis incorporating polytropic endothermic/exothermic and compression/expansion processes, presents a novel biogas fired Stirling engine-based micro-CHP system model, rigorously considering the characteristics of the system's internal

heat-to-work conversion and thermal energy transfer processes. The accuracy of SE-G submodel in evaluating the key heat-to-work conversion performance within the CHP system is verified by comparing its predictive results with experiment and other thermal model data. Subsequently, leveraging the proposed micro-CHP system model, constructal theory is introduced to conduct optimization on crucial thermal energy transfer components within the system, including the regenerator, heater, cooler, and heating boiler. The primary conclusions are summarized as follows:

1. 1 The SE-G submodel, in the derivation of the original differential equations, not only synchronously considers the alterations in the operational characteristics of the Stirling engine due to polytropic endothermic/exothermic and compression/expansion processes but also integrates the effects of irreversible factors such as heat exchanger pressure drop and imperfect regeneration, which are typically overlooked in most thermal models. Consequently, the present model can more accurately capture the transient distribution and variation of the internal physical fields of the prime mover, thereby offering higher precision in predicting the heat-to-work conversion performance within micro-CHP systems. Given that the theoretical or empirical formulas involved in assessing thermal energy transfer processes in other submodels have been thoroughly validated in engineering practice, the micro-CHP system model proposed in this paper can be deemed reliable.
2. 2 As the length and porosity of the regenerator increase, the thermal-electric performance of micro-CHP systems with three different types of regenerators (cross-flow, parallel-flow, and inclined-flow regenerators) undergoes significant variations due to the differing heat and mass transfer characteristics of these regenerators. Overall, the optimal ranges of length and porosity for the three types of regenerators are low length and high porosity, high length and low porosity, and moderate length and low porosity, respectively. Compared to the former two types of regenerators, the inclined-flow regenerator applied in micro-CHP systems can achieve moderate electrical power output and high heat output efficiency, thereby realizing the highest comprehensive thermal-electric performance.
3. 3 With the increase in the number of heat exchange tubes in both the heater and the heating boiler, the comprehensive thermal-electric performance of the micro-CHP system exhibits an initial rise followed by a decline, suggesting the presence of an optimal tube number within the range of studied parameters. Conversely, reducing the length of tubes in the heater and increasing the number of baffles in the heating boiler result in a monotonic increase in the maximum comprehensive performance associated with the optimal number of heat exchange tubes. However, unlike the heater and the heating boiler, variations in the number and length of heat exchange tubes within the cooler have minimal impact on the overall system performance.
4. 4 After the constructal optimization, the micro-CHP system achieves an electrical power output of 6274 W, accompanied by heat output efficiency and total efficiency of 93.7 % and 96.3 %, respectively. Compared to its performance before optimization, the system's electrical power output increases by 142.8 %, while the heat output efficiency and total efficiency increase by 20.5 % and 10.5 %, respectively, resulting in a comprehensive performance index F of 4.9. This confirms the feasibility of the novel Stirling engine-based micro-CHP system model proposed in this paper for evaluating and optimizing the comprehensive thermal-electric performance of the system.

CRediT authorship contribution statement

Minjie Yu: Writing – original draft, Visualization, Validation, Software, Methodology, Investigation, Formal analysis, Data curation, Conceptualization. **Haichuan Cui:** Writing – review & editing, Validation, Software, Methodology. **Lei Xu:** Writing – review & editing, Software, Methodology. **Zhichun Liu:** Writing – review & editing, Supervision, Resources, Project administration, Funding acquisition. **Wei Liu:** Writing – review & editing, Supervision, Resources, Project administration, Funding acquisition, Conceptualization.

Declaration of competing interest

The authors declare that they have no known competing financial interests or personal relationships that could have appeared to influence the work reported in this paper.

Data availability

Data will be made available on request.

Acknowledgements

This work was supported by the National Natural Science Foundation of China (Grant No. 51736004).

Appendix A. Supplementary material

Supplementary material to this article can be found online at https://doi.org/10.1016/j.enconman.2024.118806.

References

[1] Zhu S, Yu G, Liang K, Dai W, Luo E. A review of Stirling-engine-based combined heat and power technology. Appl Energy 2021;294:116965.
[2] Bagherian MA, Mehranzamir K. A comprehensive review on renewable energy integration for combined heat and power production. Energy Convers Manag 2020;224:113454.
[3] Martinez S, Michaux G, Salagnac P, Bouvier J-L. Micro-combined heat and power systems (micro-CHP) based on renewable energy sources. Energy Convers Manag 2017;154:262–85.
[4] Chen W-L, Huang C-W, Li Y-H, Kao C-C, Cong HT. Biosyngas-fueled platinum reactor applied in micro combined heat and power system with a thermophotovoltaic array and stirling engine. Energy 2020;194:116862.
[5] González-Pino I, Pérez-Iribarren E, Campos-Celador A, Terés-Zubiaga J, Las-Heras-Casas J. Modelling and experimental characterization of a Stirling engine-based domestic micro-CHP device. Energy Convers Manag 2020;225:113429.
[6] Schneider T, Müller D, Karl J. A review of thermochemical biomass conversion combined with Stirling engines for the small-scale cogeneration of heat and power. Renew Sust Energy Rev 2020;134:110288.
[7] İncili V, Karaca Dolgun G, Georgiev A, Keçebaş A, Çetin NS. Performance evaluation of novel photovoltaic and Stirling assisted hybrid micro combined heat and power system. Renew Energy 2022;189:129–38.
[8] Wang C, Song J, You D, Zheng W, Guo J, Zhu L. Combined heat and power plants integrated with steam turbine renovations: optimal dispatch for maximizing the consumption of renewable energy. Energy Convers Manag 2022:258.
[9] Sharf M, Romm I, Palman M, Zelazo D, Cukurel B. Economic dispatch of a single micro gas turbine under CHP operation with uncertain demands. Appl Energy 2022;309:118391.
[10] Arbabi P, Abbassi A, Mansoori Z, Seyfi M. Joint numerical-technical analysis and economical evaluation of applying small internal combustion engines in combined heat and power (CHP). Appl Therm Eng 2017;113:694–704.
[11] Lu X, Du B, Zhu W, Yang Y, Xie C, Tu Z, et al. Thermodynamic and dynamic analysis of a hybrid PEMFC-ORC combined heat and power (CHP) system. Energy Convers Manag 2023;292:117408.
[12] Kasaeian A, Nouri G, Ranjbaran P, Wen D. Solar collectors and photovoltaics as combined heat and power systems: A critical review. Energy Convers Manag 2018;156:688–705.
[13] Arsalis A. A comprehensive review of fuel cell-based micro-combined-heat-and-power systems. Renew Sust Energy Rev 2019;105:391–414.
[14] Van Erdeweghe S, Van Bael J, Laenen B, D'Haeseleer W. Optimal configuration for a low-temperature geothermal CHP plant based on thermoeconomic optimization. Energy 2019;179:323–35.
[15] Roy D, Zhu S, Wang R, González-Pino I, Herrando M, Markides CN, et al. Techno-economic and environmental analyses of a solar-assisted Stirling engine cogeneration system for different dwelling types in the United Kingdom. Energy Convers Manag 2024:302.
[16] Jiang Z, Yu G, Zhu S, Dai W, Luo E. Advances on a free-piston Stirling engine-based micro-combined heat and power system. Appl Therm Eng 2022;217:119187.
[17] Sheykhi M, Mehregan M. Comprehensive technical and economic study and optimization of a novel combined cooling heating and power system driven by a four cylinder α type Stirling engine. Appl Therm Eng 2024;236:121869.

[18] Erixno O, Rahim NA, Ramadhani F, Adzman NN. Energy management of renewable energy-based combined heat and power systems: A review. Sustainable Energy Technol Assess 2022;51:101944.
[19] Najafi G, Hoseini SS, De Goey LPH, Yusaf T. Optimization of combustion in micro combined heat and power (mCHP) system with the biomass-Stirling engine using SiO_2 and Al_2O_3 nanofluids. Appl Therm Eng 2020;169:114936.
[20] Mahian O, Mirzaie MR, Kasaeian A, Mousavi SH. Exergy analysis in combined heat and power systems: A review. Energy Convers Manag 2020;226:113467.
[21] Park J, Ko J, Kim H, Hong Y, Yeom H, Park S, et al. The design and testing of a kW-class free-piston Stirling engine for micro-combined heat and power applications. Appl Therm Eng 2020;164:114504.
[22] Chen W-L, Currao G, Li Y-H, Kao C-C. Employing Taguchi method to optimize the performance of a microscale combined heat and power system with Stirling engine and thermophotovoltaic array. Energy 2023;270:126897.
[23] Chen W-L, Sirisha V, Yu C-Y, Wang Y-R, Dai M-W, Lasek J, et al. Design and optimization of a combined heat and power system with a fluidized-bed combustor and stirling engine. Energy 2024;293:130709.
[24] Schneider T, Ruf F, Müller D, Karl J. Performance of a fluidized bed-fired Stirling engine as micro-scale combined heat and power system on wood pellets. Appl Therm Eng 2021;189:116712.
[25] Auñón-Hidalgo JA, Sidrach-de-Cardona M, Auñón-Rodríguez F. Performance and CO_2 emissions assessment of a novel combined solar photovoltaic and thermal, with a Stirling engine micro-CHP system for domestic environments. Energy Convers Manag 2021;230:113793.
[26] Mehregan M, Sheykhi M, Alizadeh Kharkeshi B, Emamian A, Aliakbari K, Rafiee N. Performance analysis and optimization of combined heat and power system based on PEM fuel cell and β type Stirling engine. Energy Convers Manag 2023;283:116874.
[27] Qiu S, Gao Y, Rinker G, Yanaga K. Development of an advanced free-piston Stirling engine for micro combined heating and power application. Appl Energy 2019;235:987–1000.
[28] Zhu S, Wang K, González-Pino I, Song J, Yu G, Luo E, et al. Techno-economic analysis of a combined heat and power system integrating hybrid photovoltaic-thermal collectors, a Stirling engine and energy storage. Energy Convers Manag 2023;284:116968.
[29] Zhu S, Yu G, O J, Xu T, Wu Z, Dai W, et al. Modeling and experimental investigation of a free-piston Stirling engine-based micro-combined heat and power system. Appl Energy 2018;226:522–33.
[30] Ni M, Shi B, Xiao G, Peng H, Sultan U, Wang S, et al. Improved simple analytical model and experimental study of a 100W β-type Stirling engine. Appl Energy 2016;169:768–87.
[31] Ahmed F, Hulin H, Khan AM. Numerical modeling and optimization of beta-type Stirling engine. Appl Therm Eng 2019;149:385–400.
[32] Kongtragool B, Wongwises S. Thermodynamic analysis of a Stirling engine including dead volumes of hot space, cold space and regenerator. Renew Energy 2006;31:345–59.
[33] Urieli I, Berchowitz DM. Stirling cycle engine analysis. Bristol: Adam Hilger LTD; 1984.
[34] Babaelahi M, Sayyaadi H. A new thermal model based on polytropic numerical simulation of Stirling engines. Appl Energy 2015;141:143–59.
[35] Bejan A. Street network theory of organization in nature. J Adv Transp 1996;30:85–107.
[36] Chen L, Feng H, Xie Z, Sun F. Progress of constructal theory in China over the past decade. Int J Heat Mass Transf 2019;130:393–419.
[37] Bejan A, Lorente S. Constructal theory of generation of configuration in nature and engineering. J Appl Phys 2006;100:041301.
[38] Gheith R, Aloui F, Ben NS. Determination of adequate regenerator for a Gamma-type Stirling engine. Appl Energy 2015;139:272–80.
[39] Yu M, Xu L, Cui H, Liu Z, Liu W. A novel approach towards the selection of regenerators for optimal Stirling engine performance based on energy and exergy analyses. Sci China Tech Sci 2024;67:295–310.
[40] Costa SC, Barrutia H, Esnaola JA, Tutar M. Numerical study of the pressure drop phenomena in wound woven wire matrix of a Stirling regenerator. Energy Convers Manag 2013;67:57–65.
[41] Yanaga K, Li R, Qiu S. Robust foil regenerator flow loss and heat transfer tests under oscillating flow condition. Appl Therm Eng 2020;178:115525.
[42] Yu M, Xu L, Cui H, Liu Z, Liu W. Characteristics and potential of a novel inclined-flow stirling regenerator constructed by sinusoidal corrugated channels. Energy 2024;288:129686.
[43] Francisco RW, Oliveira AAM. Measurement of the adiabatic flame speed and overall activation energy of a methane enriched H2/CO/CO2/N2 low heating value mixture. Intl J Hydrogen Energ 2020;45:29533–45.
[44] Vasan V, Sridharan NV, Feroskhan M, Vaithiyanathan S, Subramanian B, Tsai P-C, et al. Biogas production and its utilization in internal combustion engines - A review. Process Saf Environ 2024;186:518–39.
[45] Wi'liam RM. Stirling Engine Design Manual: Second Edition, Prepared for National Aeronautics and Space Lewis Research Center Under Grant NSG3194, DOE/NASA/3194-1 NASA CR-168088; 1983.
[46] Babaelahi M, Sayyaadi H. Simple-II: A new numerical thermal model for predicting thermal performance of Stirling engines. Energy 2014;69:873–90.
[47] Hosseinzade H, Sayyaadi H. CAFS: The Combined Adiabatic-Finite Speed thermal model for simulation and optimization of Stirling engines. Energy Convers Manag 2015;91:32–53.
[48] Hosseinzade H, Sayyaadi H, Babaelahi M. A new closed-form analytical thermal model for simulating Stirling engines based on polytropic-finite speed thermodynamics. Energy Convers Manag 2015;90:395–408.
[49] Li R, Grosu L, Li W. New polytropic model to predict the performance of beta and gamma type Stirling engine. Energy 2017;128:62–76.
[50] Udeh GT, Michailos S, Ingham D, Hughes KJ, Ma L, Pourkashanian M. A new non-ideal second order thermal model with additional loss effects for simulating beta Stirling engines. Energy Convers Manag 2020;206:112493.